Materials Chemistry and Physics 254 (2020) 123412

Contents lists available at ScienceDirect

Materials Chemistry and Physics

journal homepage: www.elsevier.com/locate/matchemphys

Direct formation of $LaFeO_3$/MCM−41 nanocomposite catalysts and their catalytic reactivity for conversion of isopropanol

Kamal M.S. Khalil[a,*], Walaa A. Elhamdy[a], Abd-El-Aziz A. Said[b]

[a] *Chemistry Department, Faculty of Science, Sohag University, P.O. Box 82524, Sohag, Egypt*
[b] *Chemistry Department, Faculty of Science, Assiut University, P.O. Box 71516, Assiut, Egypt*

HIGHLIGHTS

- The method led to nanodispersion and size confinement of $LaFeO_3$ in MCM-41 pores.
- Catalytic products of isopropanol conversion were based on dispersion case of $LaFeO_3$.
- Low $LaFeO_3$/MCM-41 w/w catalysts led to pure dehydration with 100% yield.
- High $LaFeO_3$/MCM-41 w/w catalysts calcined at high temperature led to oxidation.
- The method can be generalized for different perovskites -type mixed metal oxides.

GRAPHICAL ABSTRACT

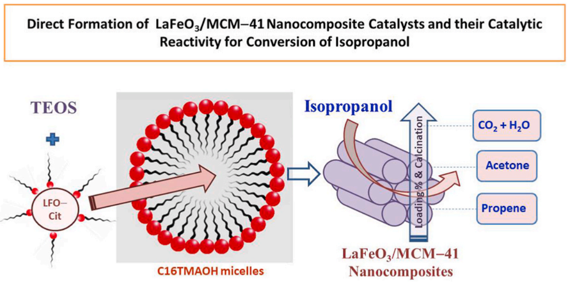

ARTICLE INFO

Keywords:
Perovskite
Mesoporous
Nanomaterials
Dehydration
Oxidation

ABSTRACT

Direct formation of 3–30% (w/w) $LaFeO_3$/MCM−41, nanocomposite catalysts were performed by a sol−gel process, followed by calcination at 550 and 750 °C. The nanocomposites were characterized through different techniques including LAXRD, WAXRD, EDX, simultaneous TG−DTA, ATR−FTIR, nitrogen adsorption/desorption, and TEM. The nanocomposites featured high surface areas (up to 1000 m^2/g) and enhanced thermal stability. The direct formation method led to nanodispersion and size confinement of $LaFeO_3$ in MCM−41 mesopores. The nanocomposites showed very high catalytic activity for isopropanol conversion, whereas their parent materials (blank MCM-41 or bulk $LaFeO_3$) were totally inactive under the same reaction conditions. Thus, nanocomposite catalysts with low loading ratios and low calcination temperature produced pure dehydration product (propene) with very high conversion and total selectivity. Nanocomposite catalysts with high loading ratios and high calcination temperature produced an appreciable amount of the dehydrogenation product (acetone) as well as the dehydration products. Moreover, high loading ratios at high reaction temperatures in air atmosphere led to the formation of oxidation products. The different reactivities of the nanocomposite catalysts were discussed and correlated to their nanostructure, in terms of enhancing of the mesoporous textures with surface acidity, oxidation ability and thermal stability.

---

* Corresponding author.
E-mail addresses: kms_khalil@yahoo.co.uk, kms_khalil@science.sohag.edu.eg (K.M.S. Khalil).

https://doi.org/10.1016/j.matchemphys.2020.123412
Received 16 May 2017; Received in revised form 30 May 2020; Accepted 11 June 2020

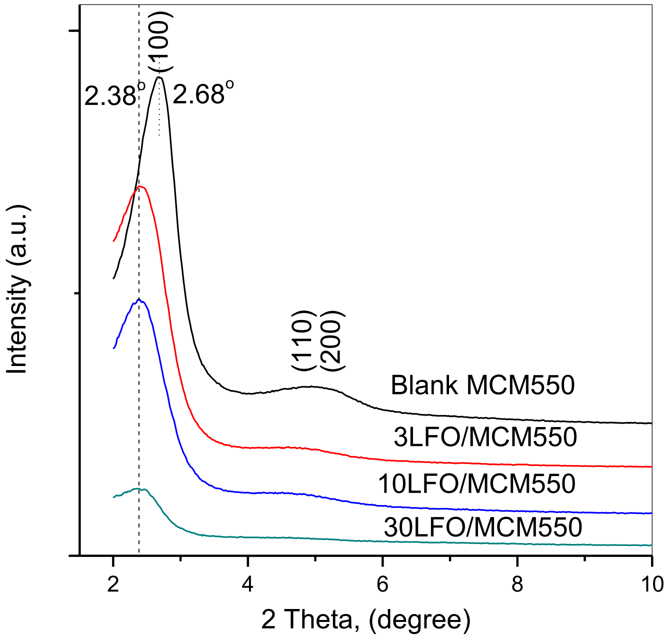

Fig. 1. Low angle XRD for the blank MCM and the composite materials calcined at 550 °C as indicated.

1. Introduction

Mixed metal oxides of perovskite-type structure (ABO_3) are very promising catalytic materials due to their high thermal stability and oxygen storage capacity [1–3]. The perovskite structure is adopted by many oxides that have the chemical formula ABO_3. $LaFeO_3$, is a typical perovskite of the general 3:3 perovskite category ($A^{3+}B^{3+}O^{2-}{}_3$). Thus, $LaFeO_3$ has been investigated as a heterogeneous catalyst for a variety of catalytic processes; including complete oxidation of benzene [4], toluene combustion [5,6], soot combustion [7], wet peroxide oxidation of organic pollutants in ambient conditions [8], methanol partial oxidation [9], and ethanol conversion [10].

Recently, some other advanced applications of perovskite-type $LaFeO_3$ have been explored; such as: visible light assisted thermocatalyst [11], photoassisted catalyst for water treatment [12], humidity resistive catalyst for effective ozone decomposition [14], photocatalytic hydrogen production from glucose [13], photo-Fenton catalytic degradation of organic dyes [15], and efficient catalytic ozonation [16].

It should be emphasized that bulk perovskite-type oxides are suffering from low specific surface area (<10 m^2/g) and poor textural characteristics. Therefore, extensive efforts have been carried out to improve their surface area and porosity [2,17–19]. To enhance surface area and other textural properties of some perovskite-type oxide, post-dispersion of some perovskite-type oxides in ordered mesoporous materials (MCM-41 or SBA-15) were reported [20–26]. Basically, the utilization of ordered mesoporous materials as a dispersion media for many active single oxides is a well-known approach towards designing of many active catalytic materials with improved textural properties [27–29]. In addition, utilization of ordered mesoporous materials, e.g. MCM-41, as a dispersion media takes the advantages of high surface areas, large pore volumes, and very uniform porosity of narrow pore size distributions. Moreover, introducing of some respective metal oxide nanoparticles in MCM-41, lead to increasing of acidity, oxidation ability and hydrothermal stability [30,31].

The present work utilizes the direct dispersion approach for $LaFeO_3$ precursors in freshly prepared MCM-41 particles, as a high porous matrix. The aim is to disperse $LaFeO_3$ phase to generate catalytically active nanocomposites that benefit from perovskite-type structure as well as high surface area and porosity of MCM-41. Catalytic reactivity of the formed nanocomposites was explored for the conversion reaction of isopropanol. The catalytic activity results were correlated to the $LaFeO_3$/MCM-41 nanocomposits texture and structure.

2. Experimental

2.1. Materials

2.1.1. Chemicals

Iron(III) nitrate nonahydrate, $Fe(NO_3)_3{\cdot}9H_2O$, 98% (+), solid product of (Prolabo, France); lanthanum(III) nitrate hexahydrate, La $(NO_3)_3{\cdot}6H_2O$; citric acid, $C_6H_8O_7$ (Merck, India); tetraethyl orthosilicate, $Si(OC_2H_5)_4$, (TEOS), 98%, liquid, (Sigma-Aldrich, Germany); cetyltrimethylammonium bromide, $CH_3(CH_2)_{15}N(Br)(CH_3)_3$, cationic surfactant ($C_{16}$TMABr); ethyl alcohol C_2H_5OH, 99.5%, (Adwic, Egypt), and aqueous ammonia solution 33% NH_3 (BDH, Ltd., England) were purchased and used as received.

2.1.2. Preparation of blank MCM−41 silica

MCM−41 was prepared according to the room temperature methods by Khalil [32] and Grün et al [33]. In the method, C_{16}TMABr was dissolved in an aqueous solution, which containing ammonia and ethanol. After dissolution TEOS was added and stirred for 1 h to produce freshly prepared MCM−41 silica sols, which utilized in the composite preparation, see below. Dried MCM−41 was obtained by filtration and drying of the freshly prepared MCM−41 silica sol overnight at 90 °C. *The resulted dry material was termed uncalcined blank MCM90.* Portions of the *dried material* were calcined at ramp rate 1 °C/min at 550 °C or 750 °C for 3 h, the resulted calcined materials were termed as blank MCM550 *or* MCM750, respectively.

2.1.3. Preparation of pure $LaFeO_3$

$LaFeO_3$ of perovskite-type, mixed metal oxides structure was prepared by a sol−gel method [34] in lights of the method described by Qi et al. [35]. In the method, $LaFeO_3$ was prepared according to the stoichiometric composition of Fe $(NO_3)_3{\cdot}9H_2O$: La $(NO_3)_3{\cdot}6H_2O$: $C_6H_8O_7$ in 50 ml of distilled water solution. The resulted solution was adjusted to *p*H 8.0 by the addition of ammonia solution to produce La–Fe–O-Citrate complex, which utilized as a precursor in the composite preparation, see below. The dried materials were obtained by aging, filtration and drying of La–Fe–O-Citrate complex was termed as $LaFeO_3$ (LFO) *uncalcined* precursor. Portions of the LFO *uncalcined* precursor was calcined at 550 °C or 750 °C, for 3 h. The resulted calcined materials were termed as LFO550 -and LFO750, respectively.

2.1.4. Preparation of LaFeO3/MCM−41 nanocomposites

A series of composite catalysts containing 3–30% $LaFeO_3$/MCM−41, w ($LaFeO_3$)/(w ($LaFeO_3$) +w (MCM)) were prepared as follows. A calculated amount of the mixed oxide precursor corresponding to 3–30% $LaFeO_3$ was prepared by reacting the stoichiometric composition of Fe $(NO_3)_3{\cdot}9H_2O$, La $(NO_3)_3{\cdot}6H_2O$ and $C_6H_8O_7$ in 50 ml of distilled water solution. The resulted solution was adjusted to *p*H 8.0 by the addition of ammonia solution and transferred directly to a beaker containing freshly prepared MCM−41 silica sol, which was prepared by the method described above. The solution was magnetically stirred at *ca.* 400 rpm and kept at this stirring rate for 1 h. The resulted solution was covered and aged for a week at room temperature. The precipitate thus obtained was filtered off and then dried overnight at 90 °C. The resulted materials were termed *uncalcined* 3–30 LFO/MCM 90. Portions of the uncalcined materials were calcined at ramp rate 1 C/min up to 550 °C or 750 °C for 3 h. The resulted materials were termed as calcined 3–30 LFO/MCM 550 and 3–30 LFO/MCM 750, respectively.

2.2. Characterization techniques

X-ray powder Diffractometry, Wide Angle and Low Angle (WAXRD

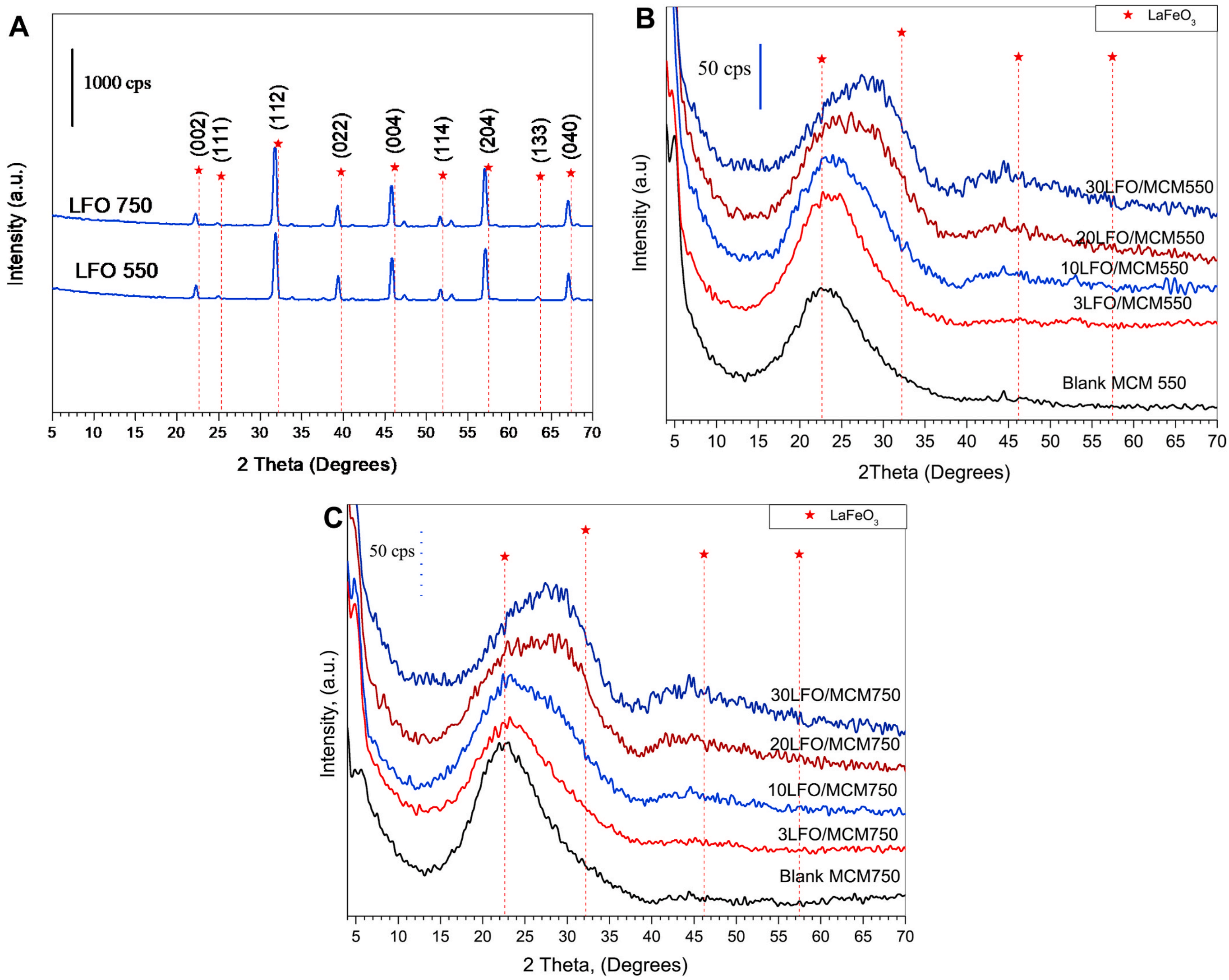

Fig. 2. XRD patterns for $LaFeO_3$ (LFO) materials obtained by calcination at 550 and 750 °C (A), as well as the blank MCM and 3-30 LFO/MCM nanocomposite materials calcined at 550 °C (B) and calcined at 750 °C (C) as indicated.

and LAXRD), patterns were obtained using a spectrometer (Phillips, model PW 2103/00, Germany) equipped with a Ni-filter, employing CuK_α radiation ($\lambda = 1.5418$ Å). The generator was operated at 35 kV and 20 mA. The diffraction patterns were indexed with the relevant standards, Joint Committee on Powder Diffraction Standards (JCPDS) for identification and indexing purposes [36]. For Low Angle–XRD (LAXRD) patterns the unit cell parameter (a_o) was calculated from the low angle diffraction pattern using the formula $a_o = 2 \times d_{100}/\sqrt{3}$, where d_{100} represented the d-spacing value of the (100) diffraction peak in low angle XRD patterns of the samples. The elemental composition and stoichiometry was checked by Energy Dispersive X-ray Spectroscopy (EDXS) measurements.

Simultaneous Thermogravimetric–Differential (TG–DTA) thermal analyses were carried out using a simultaneous thermal analyzer; (Shimadzu, model DGA-60H, Japan). TGA and DTA thermograms were recorded upon heating up from room temperature, RT, to 750 °C at a ramp rate of 10 °C/min, in the flow of nitrogen or air atmosphere at 40 ml min^{-1}.

Attenuated Total Reflectance–Fourier Transforms Infrared (ATR–FTIR) Spectroscopy of the test samples were recorded in the range of 400–4000 cm^{-1} using spectrometer (Bruker-Alpha FT-IR, Germany) equipped with a ZnSe ATR crystal.

Nitrogen Adsorption/Desorption Isotherms were measured at −196 °C using an automated instrument (Micromeritics, model ASAP 2010 instrument, USA). Prior to measurement, test samples were degassed for 2 h at 200 °C to 0.1Pa. The specific surface area, S_{BET}, was calculated by applying the Brunauer–Emmett–Teller (BET) equation [37]. Pore width distribution over the mesopore range was generated by the Barrett-Joyner- Halenda (BJH) [38], all the measurement and related analyses were preformed in lights of the IUPAC regulations [39].

Transmission Electron Microscopy (TEM) micrographs were obtained by using an electron microscope (Joel, model 2000, Japan) operated at 100 kV. Before testing, samples were prepared by ultrasonic dispersion of the solid in ethanol. A drop of the resulting suspension was dropped onto a carbon-coated copper mesh grid and allowed to dry in a drying furnace before testing.

2.3. Catalytic activity measurements

Heterogeneous catalytic activity of the nanocomposites under investigation for the vapor–phase dehydration of isopropanol was carried out in a conventional fixed-bed flow type glass reactor at atmospheric pressure using N_2 gas (or air) as a carrier gas. The catalytic system consists of two tube reactors. One charged with the catalyst, and the other used as a blank reactor i.e. without catalyst and acted as a blank reactor to measure un-catalyzed reactant conversion (if any). The

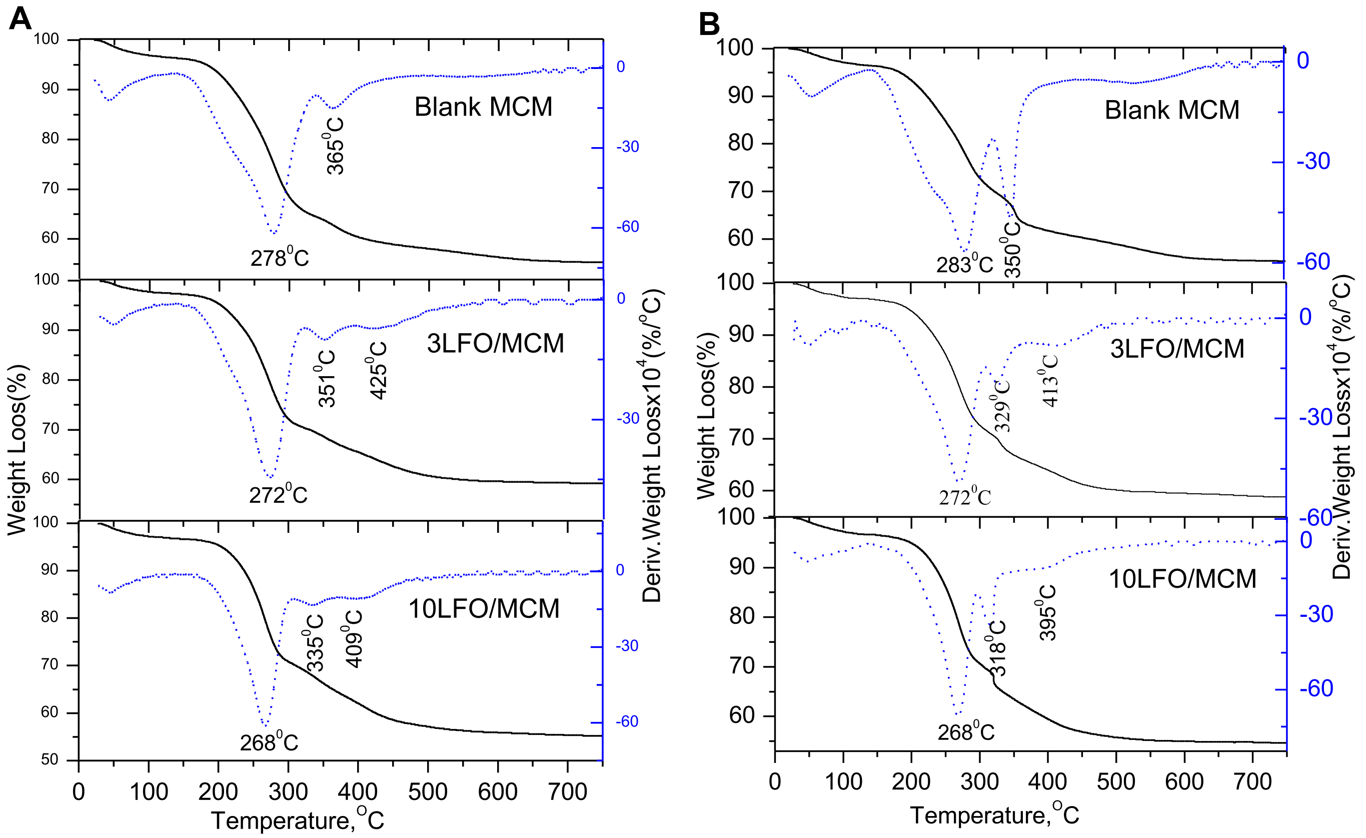

Fig. 3. TGA along with DTG curves for the uncalcined (dried at 90 °C) materials, in the flow of N_2 gas (A) and the flow of air atmosphere (B), as indicated.

charged reactor contains a weighted amount of the catalyst (optimized to 0.300 g), which held with a quartz wool bed in the middle of the reactor. The spaces in the reactor pre– and post–heating zone were filled with glass beads to reduce the effect of auto–oxidation of the substrate and products in the gas phase. The system reactors (charged and blank) were placed very close to each other in a tubular furnace. Temperature was controlled and measured using a K-type thermocouple placed in the center of the furnace and just above the catalyst bed. Isopropanol vapor and air were introduced into the reactor after air was bubbled through the isopropanol saturator. The total flow rate was fixed at 50 ml min^{-1} containing 2.0% isopropanol in the gas feed. The flow rate was measured and controlled by a Dwyer mass flow controller (series GFC, USA). The gas products were analyzed by a Unicam Pro Gas chromatograph with FID detector, using a 2.0 m DNP glass column for standard analysis of the reaction products of isopropanol on the tested catalysts. Measurements of the conversion and yield (%) were recorded after 1 h from the initial introduction of the reactant into the reactor to ensure the attainment of the reaction equilibrium steady–state conditions for the catalytic reaction. A typical setup has been previously employed for dehydration of alcohol [40]. Similar procedure for the catalytic conversion of isopropanol was described by Ogo et al. [41].

3. Results and discussion

3.1. Structural characteristics of the formed nanocomposites

LAXRD patterns obtained with the formed blank MCM550 material, Fig. 1 (A), shows a few Bragg peaks at low angles (2θ) between 2.3 and 7.0°. These peaks were indexed as (100), (110) and (200) of the hexagonal system of MCM-41 structure [42]. The corresponding LAXRD patterns for 3–30 LFO/M550 composite materials showed clearly the (100) peak and the intensity of this peak was decreased with increasing of the LFO loading ratio. The other low angle peaks were largely lost for the high loading ratio composite materials. Similar observations were reported for rare earth post-loaded MCM-41 materials [42].

Wide angle XRD patterns (WAXRD) for the pure mixed oxide $LaFeO_3$ (LFO) obtained by calcination at 550 and 750 °C are shown in Fig. 2 (A), The patterns are in complete agreement with data reported for perovskite type mixed oxide, $LaFeO_3$ (JCPDS-No.74–2203) [36]. The intensity of the XRD peaks increase with increasing of the calcination temperature from 550 °C to 750 °C as expected.

XRD for 3–30 LFO/M550 and 750 composites along with the corresponding blank MCM materials are shown in Fig. 2. (B and C), respectively. Generally, all the calcined materials with various loading ratios were influenced by amorphous nature of the MCM−41 silica, especially for low loading ratios (3 and 10LFO). No Sharpe peaks were detected neither for $LaFeO_3$, nor for the other most possible single oxides, La_2O_3 and Fe_2O_3 (hematite), (file No. 38–1355 and No. 33–0664, respectively) [36]. However, some lines broadening were detected for the most evident peak positions for $LaFeO_3$ for the high loading ratios nanocomposites. These results indicated that highly dispersed, small nano-sized particles of $LaFeO_3$ were formed, which were either amorphous or very small crystallites (below the detection limit of the XRD). This result coincides with that reported [43] for a citrate precursors of $LaCoO_3$ supported on pre-prepared MCM-41, and calcined at 600 °C. Moreover, the formation of perovskite oxide ($LaFeO_3$, $PrFeO_3$ and $LaCoO_3$) nanoparticles supported on ordered mesoporous silica with different pore geometry (gyroidal, cylindrical, spherical) and pore size (7.5, 12, 17 nm) were investigated [44]. It has been concluded that fast nucleation and crystallization fostered in small size gyroidal or cylindrica pores (where small domains of metal oxides precursors were infiltrated) and led to amorphous ABO_3 phase. Whereas, slow crystallization occurred in wide spherical pores (where large domains metal oxides precursors were infiltrated) and produced well crystalline ABO_3 structure [44].

The elemental analysis and stoichiometry of the formed materials

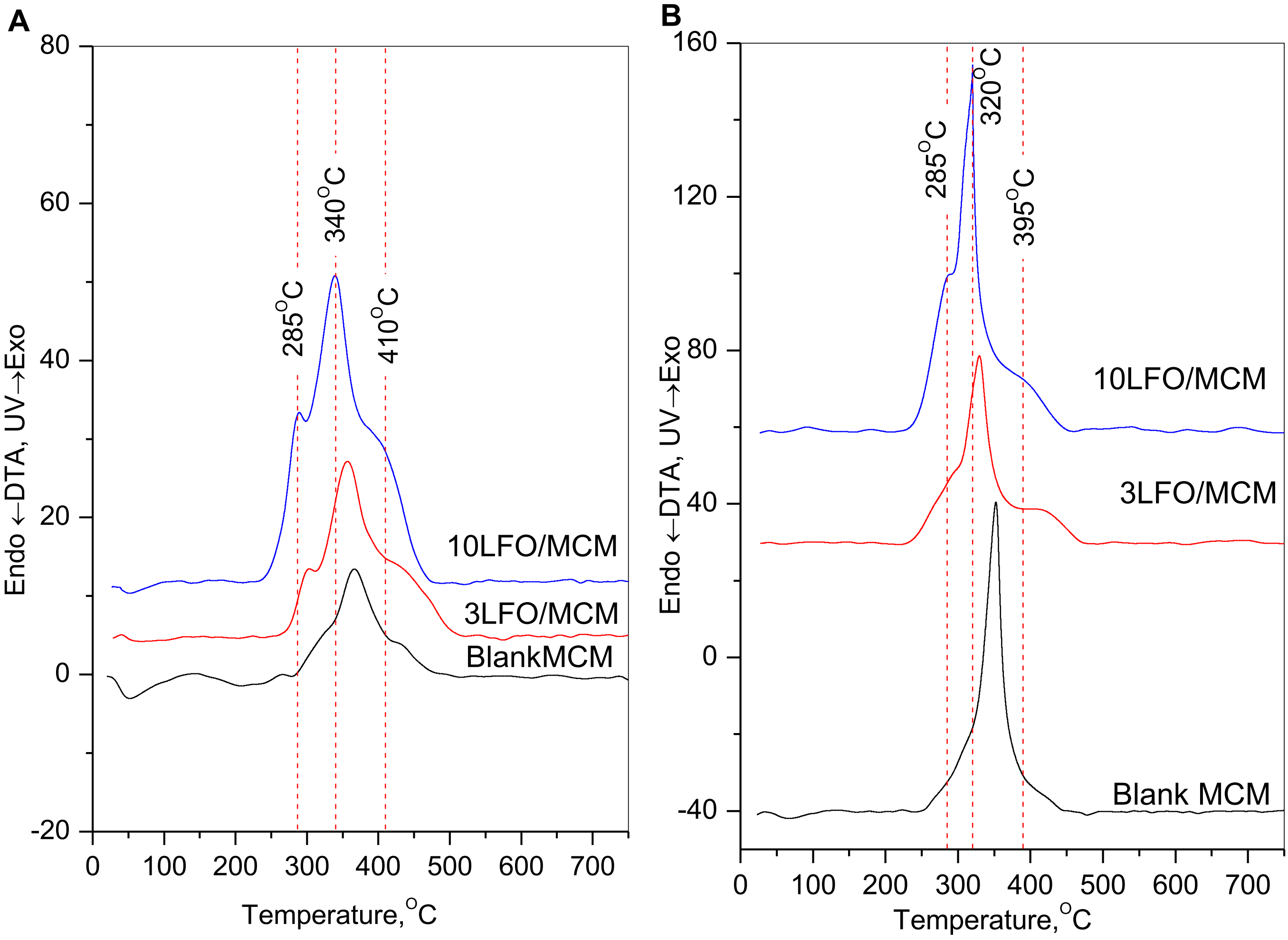

Fig. 4. DTA curves for the uncalcined (dried at 90 °C) materials, in the flow of N_2 gas (A) and in the flow of air atmosphere (B), as indicated.

were determined from EDXS measurements. The EDXS patterns obtained with blank MCM-41, 10 and 30LFO/MCM 750, showed that only silicon (Si), lanthanum (La), iron (Fe) and oxygen (O) were present. The K_α peaks at around 1.74 keV was related to Si, peak at around 4.65 keV was related to La and peak at around 6.40 keV to Fe. The position and integration of the observed peaks proved the targeted composition of the nanocomposites within the accuracy of the method.

3.2. Thermal evolution of the nanocomposites from their precursors

To investigate the way LFO−citrate complex affected the evolution of the formed structures, thermal decomposition course of the uncalcined LFO/MCM-41 nanocompoites was investigated in relation to their parent materials. TGA and DTG curves for the uncalcined blank MCM-41, in the flow of N_2 or air atmosphere are shown in Fig. 3 (A and B), respectively. Total weight loss recorded over the temperature range of RT−750 °C was 44.7% in the flow of N_2 and (44.6% in the flow of air) atmosphere. This weight loss, due to elimination of the surfactant and development of the MCM-41 structure, occurred through a process of four steps [34], in flow of N_2 or air.

The TGA and DTG curves for the formation of 3 and 10 LFO/MCM in the flow of N_2 or air atmosphere are shown in Fig. 3 (A and B). The evolution of composite material also occurred through the four-step process, however, the third step can be divided into two sub-steps (IIIa and IIIb) due to the presence of LFO precursors. Thus, for 10 LFO/MCM, the main derivative weight losses (DTG) appeared at 268, 335 and 409 °C in the flow of N_2 (or at 268, 318 and 395 °C in the flow of air). It is clear that the first peak was observed at 268 °C in N_2 or air flow, thus indicating a decomposition rather than combustion nature. Whereas, the other two peaks at 335 and 409 °C were shifted to lower temperatures (318 and 395 °C), which, indicates their combustion nature.

The simultaneous DTA curves for the above unclaimed materials are shown in Fig. 4 (A and B). The blank material showed one main peak at 360 °C with a small shoulder at 430 °C in the flow of N_2 (one main peak at 353 °C in flow of air). For the 10 LFO/MCM composite precursor materials, three exothermic features can be resolved at 285, 340 and 410 °C in the flow of N_2 (or at 285, 320, 390 °C in the flow of air). The first DTA peak appears at the same position, either in the N_2 gas flow or air flow (non-combustion event). Whereas, the other two peaks were facilitated in flow of air, indicating a combustion event. It should be noted that no other peaks were observed at higher temperatures.

The evolution of the targeted nanocomposites from their precursors upon calcination was traced by FTIR spectroscopy of the solid phase materials before and after calcinations. Thus, ATR−FTIR spectra of the uncalcined blank and composite materials 3–30 LFO/MCM 90 are shown in Fig. 5 (A). The spectra show several bands characteristic for the MCM-41 precursor material [45–47]. The observed bands were grouped into three groups (indicated by Roman numbers I, II and III) to simplify their indexing process. Thus, group (I) is related to the surfactant molecules (the weak bands at 2928, and 2856 cm^{-1} assigned for ν CH(-CH_3) and ν CH(-CH_2-); the band at 1475 cm^{-1} assigned for δ CH(-CH_3) and δ CH(-CH_2-) groups [48]. Group (II) showed two bands at 1570 and 1420 cm^{-1} which assigned for ν_{as} (COO^-) and ν_s (COO^-), and the large difference between the two modes is indicative of bi-dentate nature. One

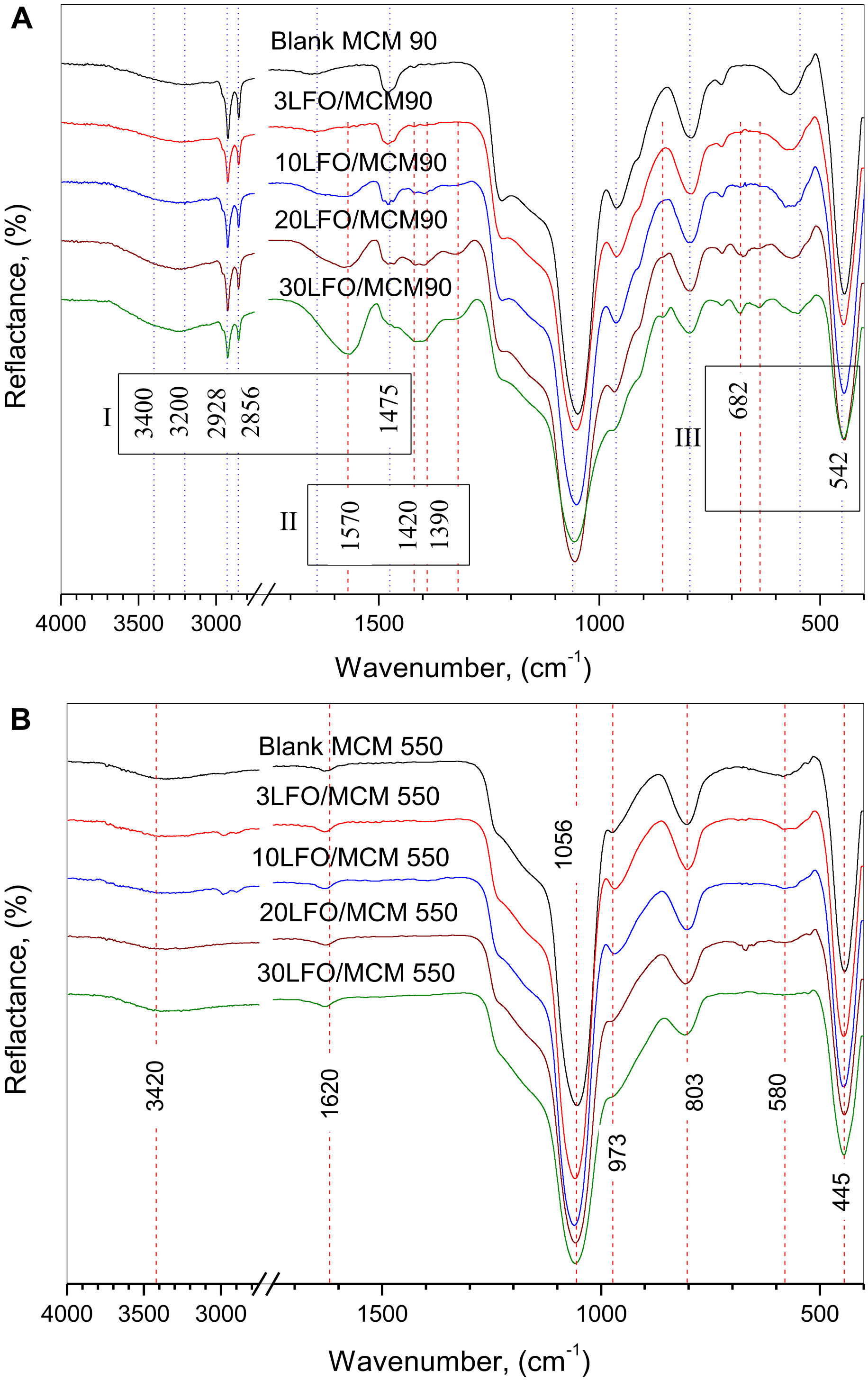

Fig. 5. ATR-FTIR spectra for the uncalcined (dried at 90 °C) materials (A), along with the materials calcined at 550 °C(B) and calcined at 750 °C (C), as indicated.

more band in this group is shown at 1390 cm^{-1}, which assigned for adsorbed ammonia and/or nitrate species. Group (III) showed two bands at 682 and 542 cm^{-1}, which assign for ν (Fe–O) in $LaFeO_3$ system Hosseni [49]. Group (IV) showed as few bands below 1400 cm^{-1}, which relate to the framework vibration of silica materials. Namely, the bands at 1224 and 1060 cm^{-1} assigned to ν_{as} (Si–O–Si); the band at 960 cm^{-1} assigns to ν_{as} (Si– OH); the band at 795 cm^{-1} assigned to ν_s (Si–O–Si); and the band at 450 cm^{-1} assigned to δ(Si–O–Si). Two more bands were observed at 3400 and 3200 cm^{-1}, which assigned to adsorbed water and ammonia.

ATR- FTIR spectra for the claimed blank and 3–30 LFO/M 550 and 750 composites are shown in Fig. 5 (B and C). All the bands related to the surfactant and citrate precursor were completely removed by calcination. The spectra showed only bands related to MCM-41 silica framework structure (group IV). Nevertheless, the intensity of the band related to Si–OH ν (973 cm^{-1}) was little decreased with increasing of the LFO ratio. This decrease in the intensity of Si–OH vibration indicates gradual surface modification of the silica surface.

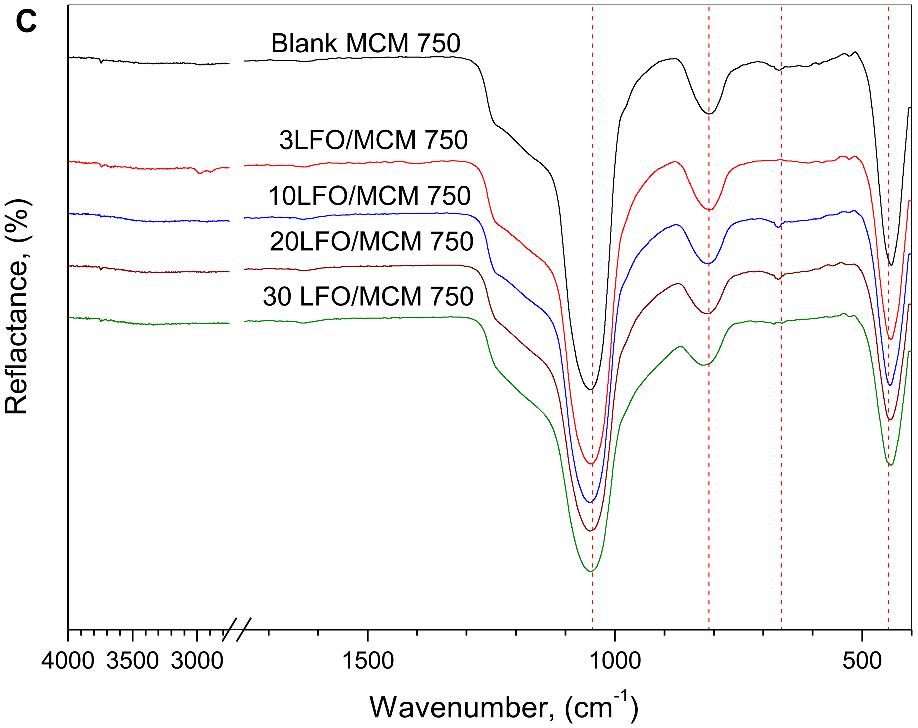

Fig. 5. (*continued*).

3.3. *Textural assessment of the nanocomposites*

Textures of the calcined nanocomposites in relation to calcined bulk LFO and blank MCM materials were investigated by nitrogen adsorption/desorption technique. Isotherms for the calcined blank MCM550 and MCM750 are shown in Fig. 6 (A), which can be classified as type IV of isotherm, characteristic for MCM-41 materials [50]. Specific surface area values were amounting to 1157 and 1143 m^2 g^{-1} for the calcined blank MCM550 and MCM750, respectively. On the other hand, for the calcined pure LFO550 and LFO750 , very low specific surface area values amounting to 4.1 and 3.5 m^2 g^{-1} were detected, respectively. Further textural details were cited in Table 1.

Isotherms for the calcined composites 3–30 LFO/MCM 550 and 750 are shown in Fig. 6 (B and C, respectively). According to the original IUPAC classification [35], the isotherms are classified as type IV of isotherms and showed characteristics of MCM-41 materials. However, the characteristic steep increase of nitrogen uptake was observed at p/p_o range 0.20–0.30, which is noticeably little higher than the range observed for their corresponding blank material, see Fig. 6 (A). This confirms widening of the small size mesopores for the composites during the formation process. This result is in agreement with the results of wide-angle XRD diffraction shown above.

Moreover, at higher relative pressure, hysteresis loops were developed in the adsorption/desorption isotherms of the claimed composite materials. The hysteresis loops were getting wider and wider with increasing of the loading ration. The hysteresis loops can be classified as type H1 for lower loading ratios composites (3 and 10 LFO/MCM) and as type H2 for the higher loading ratios composites (20 and 30LFO/MCM). This result suggests that at lower loading ratios some wider mesoporosity between compacts of uniform MCM-41 spheres would develpe (i.e. inter particle porosity). At higher loading ratios this inter particle-mesoporosity changed into networking porosity, which characterized by type H2 of isotherms. Furtheremore, according to the recent classification of adsorption isotherms [50], the isotherms of the LFO/MCM550 and LFO/MCM750 composite materials can be classified as type IV$_b$ of isotherms.

High S_{BET} values amounting to 1096, 1011, 882 and 724 m^2 g^{-1} were obtained for 3, 10, 20 and 30 LFO/MCM 550. Total pore volume, V_p, in the range of (0.808–0.689 cm^3 g^{-1}) were obtained. Whereas, S_{BET} values amounting to 1035, 954, 896 and 682 m^2 g^{-1} were obtained for 3, 10, 20 and 30 LFO/MCM 750, respectively. Total pore volume, V_p, in the range of (0.723–0.615 cm^3 g^{-1}) were obtained. Further textural data are cited in Table 1.

It is clear that the isotherms of the composite materials preserve most of the MCM-41 structure. This suggests that loading of the mixed oxide precursor led to stabilization of the MCM-41 structure against sintering upon calcination at higher temperature. Generally, the S_{BET} values decreased with increasing of the loading ratio of LFO, mainly, due to gradual pore blockage of the MCM and partial destruction of the ordered porous structure. The preservation of high surface area of the composite materials is related to high dispersion of nano sized LFO mixed oxide in MCM matrix. This situation led to preservation of most of the surface area and the surviving of MCM structure.

Moreover, S_{BET} and V_p values were little decreased with increasing of the calcination temperature from 550 to 750 °C, for all the composite ratios, see Table 1. This decrease may be attributed to filling of the pore with LFO and/or pore collapse upon calcination at the higher temperature.

As a test for micro porosity, the *t*-plot analysis was carried out on the adsorption branches of the isotherms of the calcined composite materials. The results thus obtained are cited in Table 1. Accordingly, the composite generally showed mesoporosity, however, little micro porosity were developed for the composites with high ratio composites (20 and 30%).

The average pore width of the calcined materials, W_P, was calculated via the average pore width ($4V_P/S_{BET}$) and BJH methods see Table 1. Pore size distribution for LFO/MCM 550 and 750 nanocomposites are shown in Fig. 7 (A and B), respectively. The distributions for the 3–30 LFO/MCM 550 calcined composites were maximized at 23.4–21.2 Å, compared with 19.7 Å for their blank material. The distributions for the 3–30 LFO/MCM 750 calcined composites were maximized at about 20.3–19.7 Å, compared with 18.0 Å for their blank MCM 750 material.

Transmission electron micrograph for a typical 10 and 30 LFO/MCM 750, are shown in Fig. 8 (A and B). From the images it is easy to

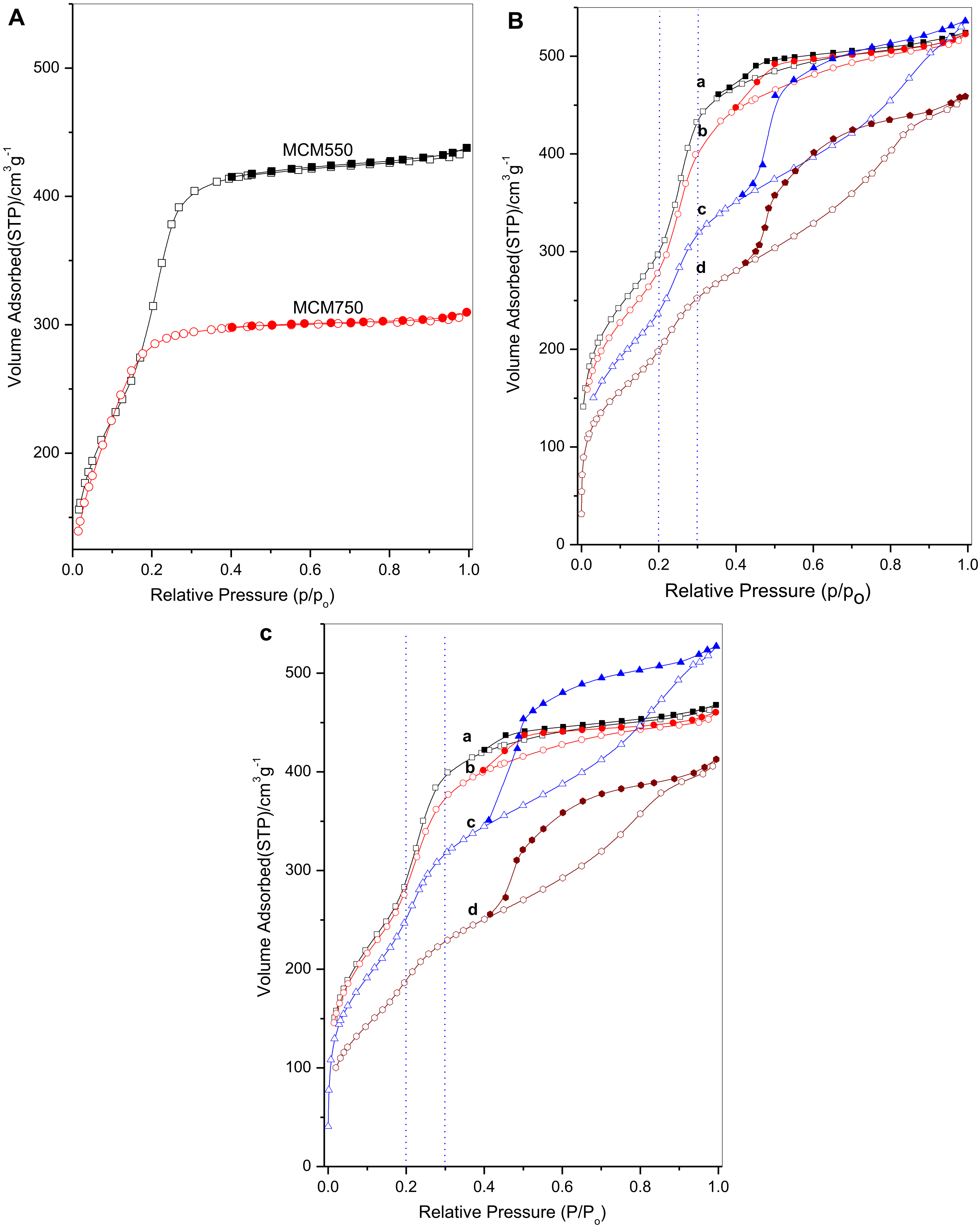

Fig. 6. N_2 adsorption/desorption isotherms for the calcined MCM550 and MCM750 blank materials (A), as well as the isotherm for 3, 10, 20 and 30 LFO/MCM550 nanocomposites indicated as a, b, c and d, respectively, calcined at 550 °C (B) and calcined at 750 °C (C).

Table 1
Textural characteristics for calcined blank MCM and 3–30 LFO/MCM nanocomposites calcined at 550 and 750 °C catalysts.

Samples	S_{BET} (m^2g^{-1})	C_{BET}	V_p cm^3 g^{-1}	*t*-method m^2 g^{-1}		Pore width W_p/Å	
				S_{mic}	S_t	4V/ S_{BET}	BJH
Blank MCM550	1157	28	0.677	0	1157	23.4	19.8
3LFO/ MCM550	1096	62	0.796	2.08	1094	29.0	23.4
10LFO/ MCM550	1011	68	0.808	0	1011	32.0	22.2
20LFO/ MCM550	882	51	0.803	0	882	36.4	22
30LFO/ MCM550	724	52	0.689	0	724	38.03	21
Blank MCM750	1143	32.3	0.480	0	1143	16.8	17.9
3LFO/ MCM750	1035	48.1	0.723	0	1035	27.9	20.2
10LFO/ MCM750	954	72.8	0.712	0	954	29.9	20.3
20LFO/ MCM750	896	48.23	0.790	0	896	35.3	20.7
30LFO/ MCM750	682	43.14	0.615	0	682	38.0	19.7

recognize the projection of regular spherical particles of the MCM-41. It is interesting to indicate that the spherical morphology of the MCM−41 materials was preserved even with the highest loading ratio in the present case without any distortion, probably due to the employing of citrate complexation reagent. Particles size was estimated in the range of 300–400 nm. Moving from 10 to 30 LFO/MCM 750 materials it is easy to recognize the presence of an increasing spread of irregular dark shadows, which represent aggregates of LFO phase within the pores of MCM. Thus, the materials morphology may be pictured as a matrix composed of spherical MCM silica particulates containing many small irregular separate or aggregated nanoparticles of LFO.

The formation mechanism of the target nanocomposite catalysts may be pictured from the above results. Thus, from TGA, DTA and FTIR results the co-existence of the LFO citrate precursor along with the CTABr surfactant in the uncalcined nanocomposite precursors; and their decomposition into metal oxide during the surfactant removal process were evident. Moreover, the presented XRD and pore width results indicated pore widening process due to the loading of LFO precursor. Thus, it is evident that the presence of LFO−citrate complex enlarged the size of the micelles that assisted the formation of MCM-41 structure. Micelles size enlargement indicats that LFO−citrate complex was encapsulated with in the surfactant micelles. Insertion of LFO−citrate complex (encapsulated by the micelles) inside NCM-41 structures was aided by the virtue of surfactant self−orientation mechanism. This led to increasing of the micelles cross section area and thereby resulted in the formation of wider pores (than the case of blank MCM-41) upon removal of the surfactant during calcination. This formation mechanism and evolution of structure is schematically represented in Scheme 1. The suggested formation and structure evolution scheme is consistent with the results shown above by TEM and N_2 adsorption isotherms.

3.4. *Catalytic conversion of isopropanol*

Catalytic activity of the formed LFO/MCM550 and LFO/MCM750

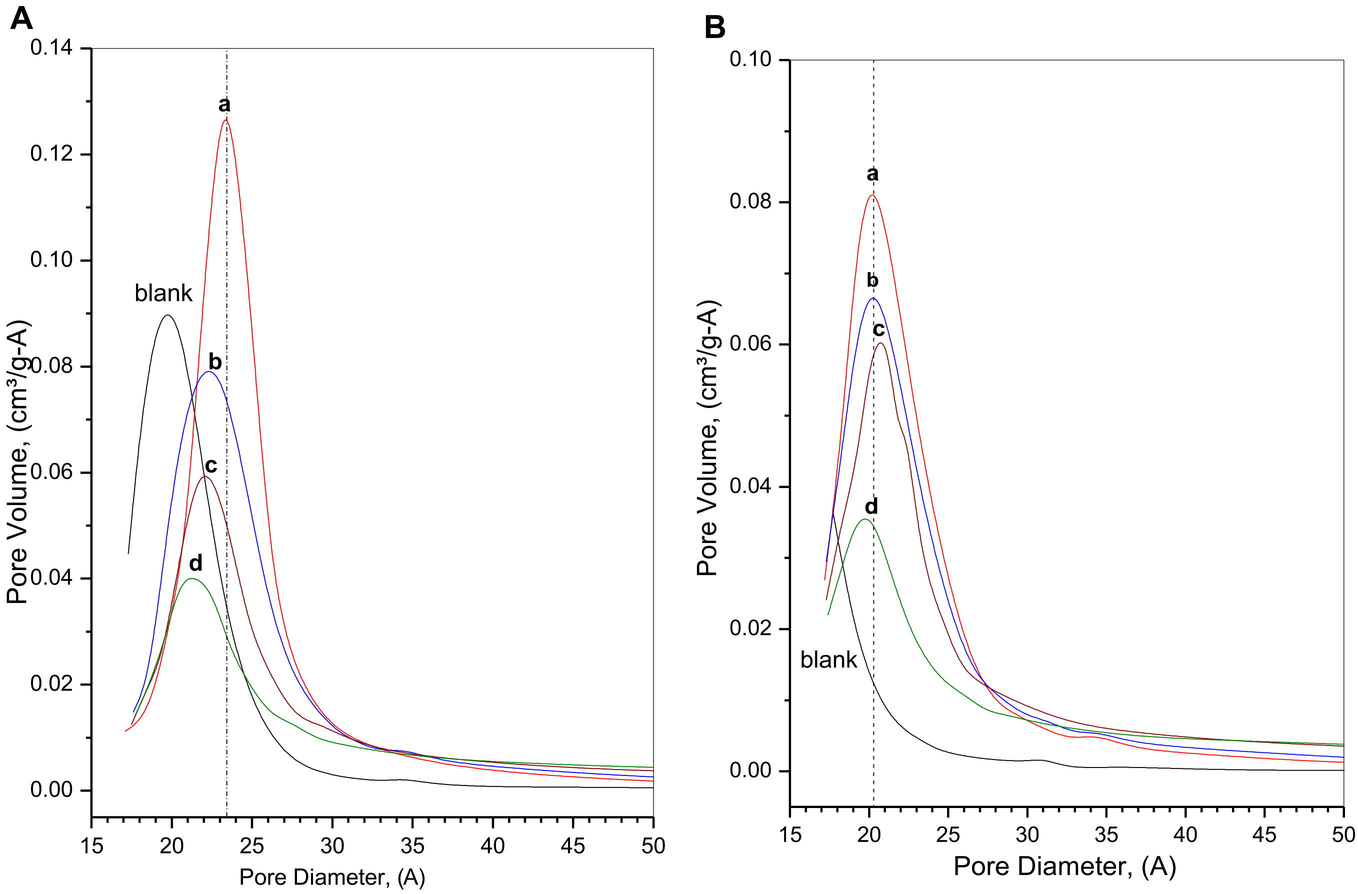

Fig. 7. Pore size distributions for the blank MCM material as well as 3, 10, 20 and 30 LFO/MCM nanocomposites indicated as a, b, c and d, respectively, calcined at 550 °C (A) and calcined at 750 °C (B).

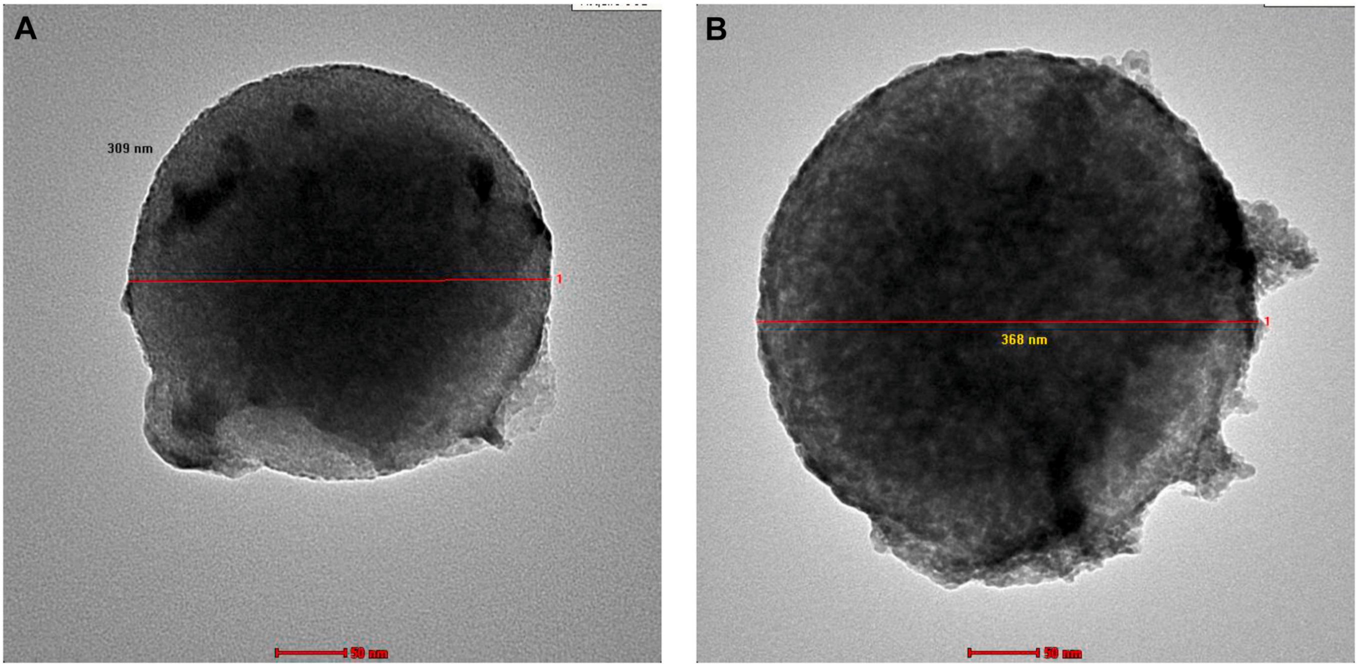

Fig. 8. TEM micrographs for the nanocomposite materials 10LFO/MCM750 (A) and 30LFO/MCM750(B).

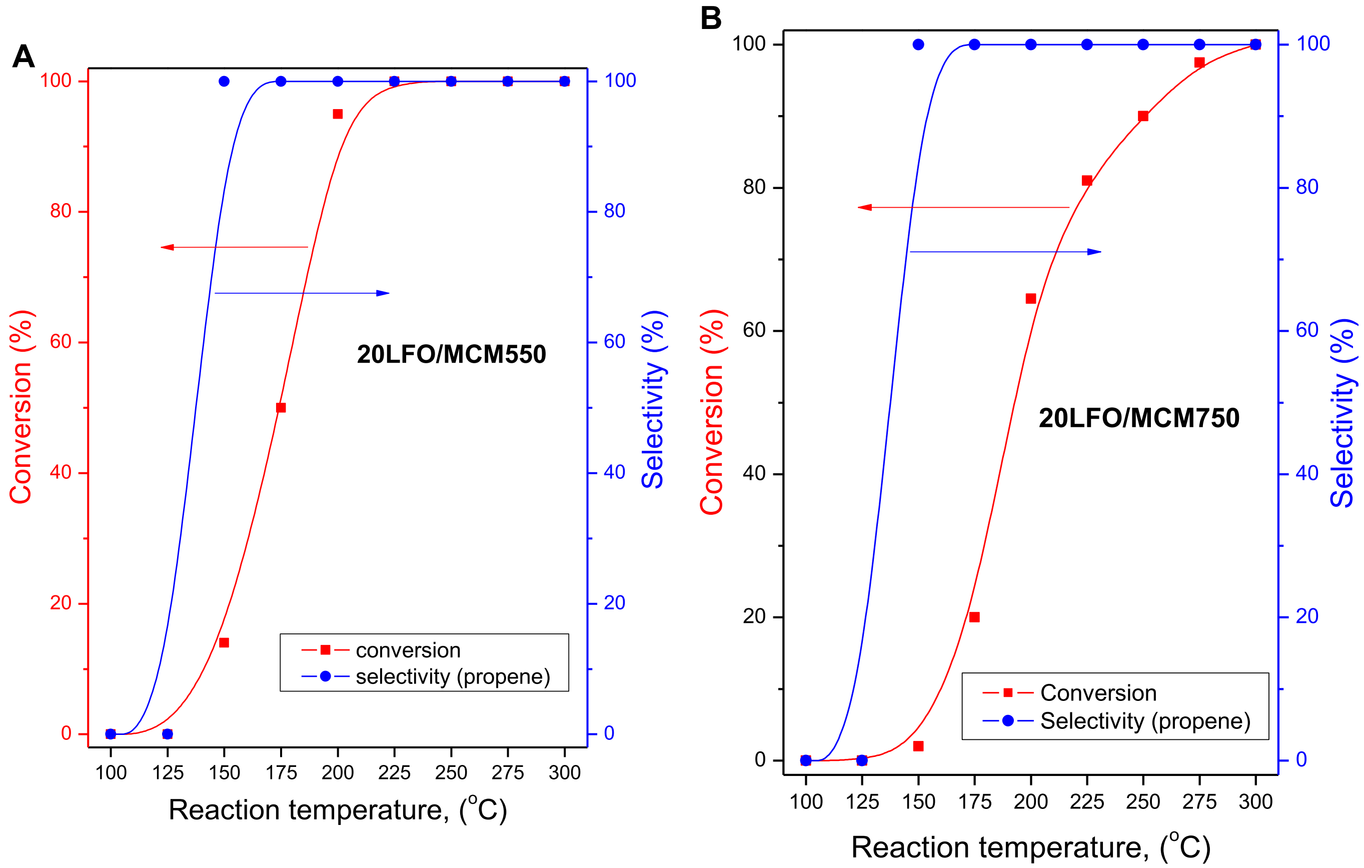

Fig. 9. Effect of reaction temperature on the catalytic activity of 20LFO/MCM550 (A) and 20LFO/MCM750 (B), nanocomposite catalysts in a flow of N_2 gas.

nanocomposite catalysts were examined for the heterogeneous conversion of isopropanol (as a small light alcohol) to gain some information about the impact of LFO dispersion in MCM-41 silica matrix. The catalytic conversion of isopropanol is generally employed as a catalytic test reaction to clarify the prevailing catalytic properties for many catalytic materials. Thus, catalysts can be classified according to their degree of acidity in dehydration (to propene) or dehydrogenation (to acetone). It was suggested that the dehydration of isopropanol to propene takes

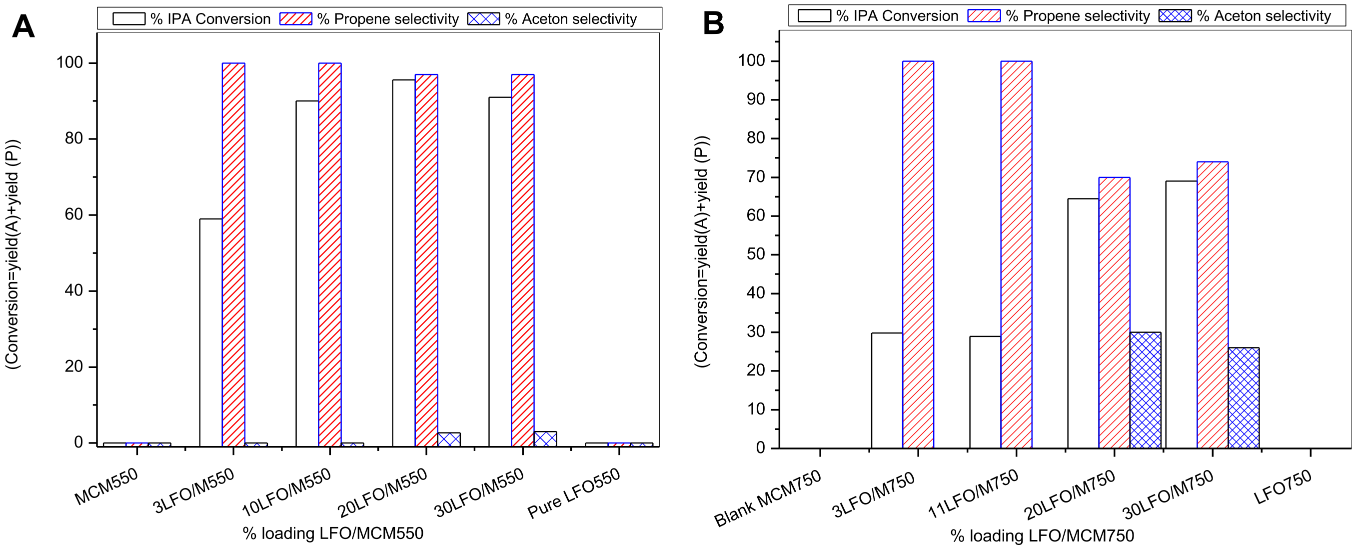

Fig. 10. Isopropanol conversion over the prepared 3-30LFO/MCM nanocomposites catalysts, along with the corresponding blank MCM and bulk LFO cacined at 550 (A) and 750 °C (B).

place on acid sites, whereas dehydrogenation to acetone is accomplished on redox or basic sites [40,51,52], for many catalytic systems.

Moreover, isopropanol conversion has been utilized to examine some MCM-41 based catalysts such as: mesoporous MCM-41 materials impregnated with Nb_2O_5 and Ga_2O_3, [53]; MCM-41 containing chromium [54]. Very recently, the conversion of isopropanol on Cr-MCM-41 catalysts has been investigated and the acid-base properties of the material were correlated with the products type and amount [55]. On the other hand, the acid-base properties of $La_{1+\chi}FeO_{3+\delta}$ perovskite and La_2O_3 have been evaluated from their isopropanol reactivity [56]. From the above studies, it has been widely agreed that (i) the dehydration of isopropanol to propene takes place on acid sites, and (ii) dehydrogenation to acetone takes place on redox sites.

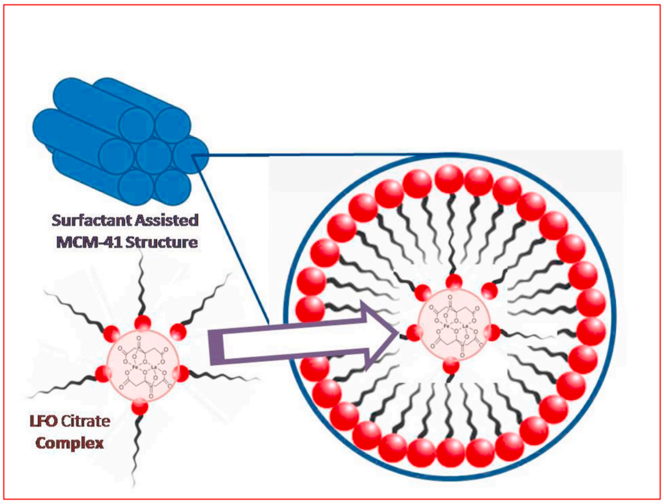

Scheme 1. Schematic representation for the formation of $LaFeO_3$/MCM-41 nanocomposite.

Catalytic activity of the calcined nanocomposites was initially tested by the catalytic conversion of isopropanol as a function of the reaction temperature in the range of 100–300 °C. To simplify the reaction mechanism and to avoid the formation of secondary products, low isopropanol concentration in the feed stream was utilized. Typical results for 20LFO/MCM 550 and 20LFO/MCM750 catalysts are shown in Fig. 9 (A and B), respectively, in a flow of N_2 gas. Results indicated that the catalytic activity onsets at a low temperature as low as 125 °C. However, isopropanol conversion increased steeply with the increasing of reaction temperature, reaches 50% conversion at 175 and 190 °C; then complete conversion at 225 and 300 °C for MCM550 and MCM750 nanocomposite catalysts, respectively. High selectivity (100%) for propene formation was observed at low temperatures and complete conversion was observed at 250 °C and at 300 °C for MCM550 and MCM750 nanocomposite catalysts, respectively. The catalytic reaction was also investigated in a flow of air as a carrier gas. Thus, higher reactivity and better catalytic stability against deactivation were observed. However, above 225 °C, increasing amounts of CO_2 and H_2O were detected in the products indicating the oxidative nature of the catalysts at high temperatures.

Isopropanol conversion over the prepared nanocomposite, blank MCM and bulk LFO was investigated at 200 °C in a flow of air. Results for the two groups of nanocomposite catalysts, 3−30LFO/MCM550 and 3−30LFO/MCM750, are shown in Fig. 10 (A and B), respectively. The presented results showed high reactivity for the various 3–30 LFO/MCM nanocomposite catalysts calcined at 550 and 750 °C. Whereas, no reactivity was detected for the corresponding blank MCM or LFO mixed oxide under the same test conditions. The nanocomposites showed increasing catalytic conversion of isopropanol with increasing of LFO loading, which maximized for 20LFO/MCM550 (>95%) then slightly decreased for the next loading ratio. Selectivity towards propene formation approached 100% for 3 and 10 LFO/MCM550. However, for the higher loading ratios, 20 and 30 LFO/MCM550, propene selectivity maintained very high value (>97%) with minor formation of acetone (<3%).

For the group of 3–30 LFO/MCM750 nanocomposite catalysts, a relatively different catalytic activity trend towards isopropanol conversion was observed, whereas no reactivity was detected for the corresponding blank MCM or LFO under the same test conditions. However, for 3 and 10 LFO/MCM750 conversion percentages amounting to 29 and 30%, respectively, were observed. Then conversion percentages approache higher values (amounting to ~ 65 and 70%) for 20 and 30 LFO/MCM750 catalysts, respectively. Moreover, selectivity towards propene formation was gradually increased from ~29% and approached 51% for 30LFO/MCM750. Meanwhile, considerable amount of acetone as a dehydrogenation product was observed with selectivity amounting to 18, 19% for 20 and 30 LFO/MCM750 nanocomposites, respectively.

Therefore, LFO/MCM nanocomposite catalysts showed very interesting catalytic properties towards conversion of isopropanol, which can be summarized as follows. (i) Catalytic dehydration at low calcination temperature and low loading ratios ($\leq$10% of LFO). (ii) Catalytic dehydration and dehydrogenation at high calcination temperature and high loading ratios ($\geq$20% of LFO). (iii) Catalytic oxidation into CO_2 and H_2O especially at high catalytic reaction temperature (>225 °C) in a flow of air.

These observed changes in catalytic activity trends of the present nanocomposite catalyst are very versatile and throw some light on the dispersion case of LFO phase in the MCM as follows. (i) Low loading ratios form small surface LFO domain which creates the surface acidity contributed for dehydration reactions. (ii) High loading ratios and high calcination temperatures form LFO domain which manifest the oxidative dehydrogenation properties of perovskite structure. (iii) High loading ratios and high calcination temperatures at high reaction temperature in air atmosphere led to the appearance of the oxidative properties of the perovskite catalysts.

This tuning of catalytic properties indicates the versatility of the prepared nanocomposite catalytics. The absence of any reactivity for the parent materials (blank MCM-41 and bulk $LaFeO_3$) under the same reaction conditions reflects the synergetic effect of MCM-41 and $LaFeO_3$ when they present in the form of nanocomposites. This confirms that introducing of $LaFeO_3$ nanoparticles in MCM-41, lead to increasing of surface acidity, oxidation ability and structural stability of the MCM-41 matrix.

4. Conclusions

The present investigation showed some interesting results,which can be concluded as follows. The direct dispersion method permits the insertion of perovskite mixed oxide, $LaFeO_3$, inside the surfactant assisted MCM-41 structure. The presence of citrate as a complex ion reagent facilitates both capsulation and insertion of the $LaFeO_3$ mixed oxide into MCM-41 texture. Nanocomposites of low loading ratios led to the formation of small surface domains of $LaFeO_3$ that creates surface acidity responsible for dehydration properties of the nanocomposite catalysts and conversion of isopropanol into propene. High loading ratios and high calcination temperatures led to the formation of larger domains of $LaFeO_3$ and appearance of the dehydrogenation and oxidative properties of the LFO/MCM nanocomposite catalysts. The presented direct dispersion method can be generalized for dispersions of other perovskite-type mixed metal oxides in MCM-41 matrix.

CRediT authorship contribution statement

Kamal M.S. Khalil: Conceptualization, Methodology, Software, Writing - review & editing. **Walaa A. Elhamdy:** Formal analysis, Writing - original draft. **Abd-El-Aziz A. Said:** Visualization, Investigation, Supervision.

Declaration of competing interest

The authors declare that they have no known competing financial interests or personal relationships that could have appeared to influence the work reported in this paper.

References

[1] Y Zhang, D.R Mullins, A Savara, Surface reactions and catalytic activities for small alcohols over $LaMnO_3$(100) and $La_{0.7}Sr_{0.3}MnO_3$(100): dehydrogenation, dehydration, and oxidation, J. Phys. Chem. C 124 (2020) 3650–3663. https://doi.org/10.1021/acs.jpcc.9b10797.
[2] B. Cai, K. Akkiraju, W.P. Mounfield, Z. Wang, X. Li, B. Huang, S. Yuan, D. Su, Y. Román-Leshkov, Y. Shao-Horn, Solid-state gelation for nanostructured perovskite oxide aerogels, Chem. Mater. 31 (2019) 9422–9429.
[3] X. Wang, K. Huang, L. Yuan, S. Xi, W. Yan, Z. Geng, Y. Cong, Y. Sun, H. Tan, X. Wu, L. Li, S. Feng, Activation of surface oxygen sites in a cobalt-based perovskite model catalyst for CO oxidation, J. Phys. Chem. Lett. 9 (2018) 4146–4154.
[4] H. Einaga, S. Hyodo, Y. Teraoka, Complete oxidation of benzene over perovskite-type oxide catalysts, Top. Catal. 53 (2010) 629–634.
[5] G. Pecchi, M.G. Jiliberto, E.J. Delgado, L.E. Cadús, J.L.G. Fierro, Effect of B-site cation on the catalytic activity of $La_{1-x}Ca_xBO_3$ (B = Fe, Ni) perovskite-type oxides for toluene combustion, J. Chem. Technol. Biotechnol. 86 (2011) 1067–1073.
[6] K. Ji, H. Dai, J. Deng, L. Song, S. Xie, W. Han, Glucose-assisted hydrothermal preparation and catalytic performance of porous $LaFeO_3$ for toluene combustion, J. Solid State Chem. 199 (2013) 164–170.
[7] J. Xu, J. Liu, Z. Zhao, G. Zhang, A. Duan, G. Jiang, C. Xu, Preparation and catalytic performance of three-dimensionally ordered macroporous perovskite-type $LaFeO_3$ catalyst for soot combustion, Chin. J. Catal. 31 (2010) 236–241.
[8] J. Faye, E. Guélou, J. Barrault, J.M. Tatibouët, S. Valange, $LaFeO_3$ perovskite as new and performant catalyst for the wet peroxide oxidation of organic pollutants in ambient conditions, Top. Catal. 52 (2009) 1211–1219.
[9] C.-L. Wang, Y.-C. Lin, Pd-integrated lanthanum-transition metal perovskites for methanol partial oxidation, Catal. Today 174 (2011) 135–140.
[10] G. Tesquet, J. Faye, F. Hosoglu, A.-S. Mamede, F. Dumeignil, M. Capron, Ethanol reactivity over La_{1+x} $FeO_{3+\delta}$ perovskites, Appl. Catal. Gen. 511 (2016) 141–148.
[11] G. Cheng, X. Tan, X. Song, X. Chen, W. Dai, R. Yuan, X. Fu, Visible light assisted thermocatalytic reaction of CO + NO over $Pd/LaFeO_3$, Appl. Catal. B Environ. 251 (2019) 130–142.
[12] P. Garcia-Muñoz, C. Lefevre, D. Robert, N. Keller, Ti-substituted LaFeO3 perovskite as photoassisted CWPO catalyst for water treatment, Appl. Catal. B Environ. 248 (2019) 120–128.
[13] S. Gong, Z. Xie, W. Li, X. Wu, N. Han, Y. Chen, Highly active and humidity resistive perovskite $LaFeO_3$ based catalysts for efficient ozone decomposition, Appl. Catal. B Environ. 241 (2019) 578–587.
[14] G. Iervolino, V. Vaiano, D. Sannino, L. Rizzo, V. Palma, Enhanced photocatalytic hydrogen production from glucose aqueous matrices on Ru-doped $LaFeO_3$, Appl. Catal. B Environ. 207 (2017) 182–194.
[15] T.T.N. Phan, A.N. Nikoloski, P.A. Bahri, D. Li, Adsorption and photo-Fenton catalytic degradation of organic dyes over crystalline $LaFeO_3$-doped porous silica, RSC Adv. 8 (2018) 36181–36190.
[16] S. Afzal, X. Quan, J. Zhang, High surface area mesoporous nanocast $LaMO_3$ (M = Mn, Fe) perovskites for efficient catalytic ozonation and an insight into probable catalytic mechanism, Appl. Catal. B Environ. 206 (2017) 692–703.
[17] S. Royer, D. Duprez, F. Can, X. Courtois, C. Batiot-Dupeyrat, S. Laassiri, H. Alamdari, Perovskites as substitutes of noble metals for heterogeneous catalysis: dream or reality, Chem. Rev. 114 (2014) 10292–10368.
[18] N. Sharma, H.S. Kushwaha, S.K. Sharma, K. Sachdev, Fabrication of $LaFeO_3$ and rGO-$LaFeO_3$ microspheres based gas sensors for detection of NO_2 and CO†, RSC Adv 10 (3) (2020) 1297–1308, https://doi.org/10.1039/C9RA09460A.
[19] K. Wang, H. Niu, J. Chen, J. Song, C. Mao, S. Zhang, et al., Immobilizing LaFeO $_3$ nanoparticles on carbon spheres for enhanced heterogeneous photo-Fenton like performance 2017, Appl. Surf. Sci. 404 (2017) 138–145.
[20] N. Yi, Y. Cao, Y. Su, W.L. Dai, H.Y. He, K.N. Fan, Nanocrystalline $LaCoO_3$ perovskite particles confined in SBA-15 silica as a new efficient catalyst for hydrocarbon oxidation, J. Catal. 230 (2005) 249–253.
[21] T.T.N. Phan, A.N. Nikoloski, P.A. Bahri, D. Li, Facile fabrication of perovskite-incorporated hierarchically mesoporous/macroporous silica for efficient photoassisted-Fenton degradation of dye, Appl. Surf. Sci. 491 (2019) 488–496.
[22] P. Xiao, J. Hong, T. Wang, X. Xu, Y. Yuan, J. Li, et al., Oxidative degradation of organic dyes over supported perovskite oxide $LaFeO_3$/SBA-15 under ambient conditions, Catal. Lett. 143 (2013) 887–894.
[23] N. Wang, X. Yu, Y. Wang, W. Chu, M. Liu, A comparison study on methane dry reforming with carbon dioxide over $LaNiO_3$ perovskite catalysts supported on mesoporous SBA-15, MCM-41 and silica carrier, Catal. Today 212 (2013) 98–107.
[24] M.-J. Suh, Y.-K. Park, S.-K. Ihm, One-pot synthesis of perovskite-type metal oxides via confined mesopore and their catalytic activity for toluene oxidation, Catal. Today 265 (2016) 210–217.
[25] K. Niu, L. Liang, J. Li, F. Zhang, Efficient encapsulation of $LaCoO_3$ perovskite in mesoporous silica induced by a chelating template, Microporous Mesoporous Mater. 220 (2016) 220–224.
[26] H. Li, J. Zhu, P. Xiao, Y. Zhan, K. Lv, L. Wu, et al., On the mechanism of oxidative degradation of rhodamine B over $LaFeO_3$ catalysts supported on silica materials: role of support, Microporous Mesoporous Mater. 221 (2016) 159–166.
[27] A. Taguchi, F. Schüth, Ordered mesoporous materials in catalysis, J Microporous Mesoporous Mater. 77 (2005) 1–45.
[28] S. Laha, Cerium containing MCM-41-type mesoporous materials and their acidic and redox catalytic properties, J. Catal. 207 (2002) 213–223.
[29] L.F. Chen, J.A. Wang, L.E. Noren, Synthesis and physicochemical properties of Zr-MCM-41 mesoporous molecular sieves and Pt/$H_3PW_{12}O_{40}$/Zr-MCM-41 catalysts, J. Solid State Chem. 180 (2007) 2958–2972.
[30] S.P. Naik, V. Bui, T. Ryu, J.D. Miller, W. Zmierczak, Al-MCM-41 as methanol dehydration catalyst, Appl. Catal. Gen. 381 (2010) 183–190.
[31] T. Haishi, K. Kasai, M. Iwamoto, Fast and quantitative dehydration of lower alcohols to corresponding olefins on mesoporous silica catalyst, Chem. Lett. 40 (2011) 614–616.
[32] K.M.S. Khalil, Cerium modified MCM-41 nanocomposite materials via a nonhydrothermal direct method at room temperature, J. Colloid Interface Sci. 315 (2007) 562–568.
[33] M. Grün, K.K. Unger, A. Matsumoto, K. Tsutsumi, Novel pathways for the preparation of mesoporous MCM-41 materials: control of porosity and morphology, Microporous Mesoporous Mater. 27 (1999) 207–216.

[34] K.M.S. Khalil, W.A. Elhamdy, A.A. Said, A.A. Elsamahy, Porous $LaFeO_3$/silica nanocomposites via sol-gel mixing involving citric acid, Colloid. Surface. Physicochem. Eng. Aspect. 506 (2016) 840–848.

[35] X. Qi, J. Zhou, Z. Yue, Z. Gui, L. Li, A simple way to prepare nanosized $LaFeO_3$ powders at room temperature, Ceram. Int. 29 (2003) 347–349.

[36] JCPDS, International Centre for Diffraction Data, PCPDFWIN, JCPDS-ICDD, 1995.

[37] S. Brunauer, P.H. Emmett, E. Teller, Adsorption of gases in multimolecular layers, J. Am. Chem. Soc. 60 (1938) 309–319.

[38] E.P. Barrett, L.G. Joyner, P.H. Halenda, The determination of pore volume and area distributions in porous substances. I. Computations from nitrogen isotherms, J. Am. Chem. Soc. 73 (1951) 373–380.

[39] K.S.W. Sing, D.H. Everett, R.a.W. Haul, L. Moscou, R.a. Pierotti, J. Rouquérol, et al., International union of pure commission on colloids and surface chemistry and catalysis "reporting physicsorption data for gas/solid systems with special reference to the determination of surface area and porosity, Pure Appl. Chem. 54 (1982) 2201–2218.

[40] A.E.A.A. Said, M.M. Abd El-Wahab, M.A. El-Aal, The catalytic performance of sulfated zirconia in the dehydration of methanol to dimethyl ether, J. Mol. Catal. Chem. 394 (2014) 40–47.

[41] S. Ogo, A. Onda, K. Yanagisawa, Hydrothermal synthesis of vanadate-substituted hydroxyapatites, and catalytic properties for conversion of 2-propanol, Appl. Catal. Gen. 348 (2008) 129–134.

[42] F. Schüth, A. Wingen, J. Sauer, Oxide loaded ordered mesoporous oxides for catalytic applications, Microporous Mesoporous Mater. 44–45 (2001) 465–476.

[43] S.V. Nguyen, V. Szabo, D. Trong On, S. Kaliaguine, Mesoporous silica supported $LaCoO_3$ perovskites as catalysts for methane oxidation, Microporous Mesoporous Mater. 54 (2002) 51–61.

[44] J. Scholz, M. Etter, D. Haas, A. Meyer, A. Kornowski, U. Sazama, S. Mascotto, Pore geometry effect on the synthesis of silica supported perovskite oxides, J. Colloid Interface Sci. 504 (2017) 346–355.

[45] V. Meynen, P. Cool, E.F. Vansant, Verified syntheses of mesoporous materials, Microporous Mesoporous Mater. 125 (2009) 170–223.

[46] S.B. Bukallah, A. Bumajda, K.M.S. Khalil, M.I. Zaki, Characterization of mesoporous VOx/MCM-41 composite materials obtained via post-synthesis impregnation, Appl. Surf. Sci. 256 (2010) 6179–6185.

[47] K.M.S. Khalil, M.M. Khalaf, H.S. Mohran, A.A. Elsamahy, Direct formation of iron oxide/MCM-41 nanocomposites via single or mixed n-alkyltrimethylammonium bromide surfactants, J. Colloid Interface Sci. 368 (2012) 56–63.

[48] I.A. Degen, Tables of Characteristic Group Frequencies for the Interpretation of Infrared and Raman Spectra, Acolyte Publ., Harrow, United Kingdom, 1997.

[49] S.A Hosseni, M.T. Sadghi-Sorkhani, L. Kafi-Ahamadi, A. Alemi, A. Niaei, D. Salari, Synthesis, characterization, and catalytic activity of nanocrystalline $La_{1-x}Eu_xFeO_3$ during the combustion of toluene, Chin. J. Catal. 32 (2011) 1465–1468.

[50] F. Rouquerol, J. Rouquerol, K. Sing, Adsorption by Powders and Porous Solids-Principles Methodology and Applications, Academic Press, London, 1999.

[51] F.M. Bautista, J.M. Campelo, A. García, D. Luna, J.M. Marinas, M.T. Siles, A. A. Romero, "Vanadyl – aluminum binary Phosphate : Al/V ratio influence on their structure and catalytic behavior in the 2-propanol conversion, Catal. Today 78 (2003) 269–280.

[52] O.A. Anunziata, A.R. Beltramone, M.L. Martínez, L.L. Belon, Synthesis and characterization of SBA-3 , SBA-15 , and SBA-1 nanostructured catalytic materials, J. Colloid Interface Sci. 315 (2007) 184–190.

[53] B. Sulikowski, I. Nowak, M. Misiewicz, M. Ziolek, A. Kubacka, V. Corte, Catalytic properties of niobium and gallium oxide systems supported on MCM-41 type materials, Appl. Catal. A: Gen 325 (2007) 328–335, https://doi.org/10.1016/j.apcata.2007.02.029.

[54] M. Brys, M. Trejda, M Ziolek, Relationship between basicity, reducibility and partial oxidation properties of chromium containing MCM-41, RSC Adv. 4 (2014) 62940–62946, https://doi.org/10.1039/c4ra10336j.

[55] P.M. Cuesta Zapata, E.E. Gonzo, M.L. Parentis, N.A. Bonini, Acidity evolution on highly dispersed chromium supported on mesostructured silica: the effect of hydrothermal treatment and calcination temperature, Microporous Mesoporous Mater. 294 (2020) 109895, https://doi.org/10.1016/j.micromeso.2019.109895.

[56] G. Tesquet, J. Faye, F. Hosoglu, A.-S. Mamede, F. Dumeignil, M. Capron, Ethanol reactivity over La1+x FeO3+δ perovskites, Appl. Catal. Gen. 511 (2016) 141–148.